



Microstructural characterization and mechanical properties of AlMg alloy fabricated by additive friction stir deposition

Zhikang Shen^{1,2,3} · Mingtao Zhang¹ · Dongxiao Li⁴ · Xinyu Liu¹ · Shaolong Chen¹ · Wentao Hou⁵ · Yuquan Ding⁶ · Zhonggang Sun⁷ · Yu Su¹ · Wenya Li¹ · Yanhong Tian³

Received: 30 August 2022 / Accepted: 19 January 2023 / Published online: 26 January 2023
© The Author(s), under exclusive licence to Springer-Verlag London Ltd., part of Springer Nature 2023

Abstract

This work investigates the microstructure characterization and mechanical properties of Al alloy fabricated by additive friction stir deposition (AFSD). Microstructure characterizations of the Al alloy 5B70 base material (BM) and build were compared using optical microscope (OM) and electron back scattered diffraction (EBSD). The hardness distribution in the direction perpendicular to the cross-section of the deposited area was systematically evaluated. Tensile tests were performed on the BM and the build using digital image correlation (DIC), and the real-time stress distribution states of the specimens were analyzed. After the tensile tests, the fracture micromorphology was characterized using scanning electron microscope (SEM). The results indicated that a high degree of recrystallization occurred in the deposition zone, where fine, equiaxed, and differently oriented grains are formed. It was found that the strength of the deposition layer was lower compared to that of the BM, but its toughness was significantly improved. Also, obvious anisotropy of mechanical properties was identified in the deposition layer.

Keywords Additive friction stir deposition · 5B70 Al alloy · Microstructural characterization · Mechanical properties

1 Introduction

Additive manufacturing (AM) technology, which could turn 3D models into physical entities, has been extensively investigated in recent years. In this technology, complex structural objects are fabricated by adding layer-upon-layer of material [1–3]. There are two categories of additive manufacturing technologies, i.e., fusion-based AM and solid-state AM [4]. In the case of fusion-based AM, high-energy heat sources (arc, laser, or electron beam, for instance) are applied under protective gas or vacuum conditions to heat metal materials, which are rapidly melted, solidified, and stacked layer by layer to form desired components [5, 6]. Fusion-based AM have shown tremendous advantages compared with traditional manufacturing methods [7–9]; however, they have manifold limitations due to solidification, especially for light metal materials such as aluminum alloys and magnesium alloys [10]. Solid-state AM such as ultrasonic additive manufacturing (UAM), cold spray additive manufacturing (CSAM), or friction-based additive manufacturing (FAM) does not cause the above-mentioned problems associated with solidification [11–13], since the bulk material does not melt during the whole process [14].

✉ Zhikang Shen
z45shen@uwaterloo.ca

✉ Wenya Li
liwy@nwpu.edu.cn

¹ Shaanxi Key Laboratory of Friction Welding Technologies, Northwestern Polytechnical University, Xi'an 710072, China

² College of Engineering and Technology, Southwest University, Chongqing 400715, China

³ State Key Laboratory of Advanced Welding and Joining, Harbin Institute of Technology, Harbin 150001, China

⁴ Department of Mechanical Products, Beijing Spacecrafts, Beijing 100094, China

⁵ College of Mechanical Engineering, Zhejiang University of Technology, Hangzhou 310012, People's Republic of China

⁶ Centre for Advance Materials Joining, University of Waterloo, Waterloo N2L, 3G1, Canada

⁷ College of Materials Science and Engineering and Tech Institute for Advanced Materials, Nanjing Tech University, Nanjing 211816, China

In 2012, additive friction stir deposition (AFSD) was proposed by MELD Manufacturing Company based on the basic principle of friction stir welding (FSW). As shown in Fig. 1a, a hollow and rotating tool is applied to deposit the metal powder or wire on the substrate sheet material. The feed material is softened by the frictional heat of the rotating tool, whose temperature does not reach the melting points. Therefore, AFSD can avoid the formation of porosity, thermal cracking, and ablation of alloying elements [15, 16]. The material undergoes severe plastic deformation and thus generates dynamic recrystallization (DRX). Meanwhile, the rotating tool has a strong stirring effect on the deposited material, promoting the formation of fragmentation and redistribution of the metal particles [17, 18]. In FSW and friction stir spot welding (FSSW), the frictional heat is generated mainly between the tool and workpiece materials [19–23]. However, the frictional heat in AFSD derives from the interfaces between deposited material and tool, as well as deposited material and substrate. Although no melting occurs in the as-deposited material, temperatures are high enough to cause the dissolution of strengthening phases in the filler feedstock [24–27].

Garcia et al. investigated the heat generation mechanism during AFSD of Cu and Al–Mg–Si alloys. In the deposition zone of Cu, the tool and the deposited material are in a complete slipping state, and the main heat generation comes from interfacial friction. In the case of Al–Mg–Si, the interfacial friction is partial slipping, and the heat originates from both interfacial friction and volumetric energy dissipation [28, 29]. Moreover, Griffiths et al. observed that a large amount of material rotation and larger transition zone boundaries were

identified in the deposition zone of Al–Mg–Si, indicating that the surface area and friction coefficient of Al–Al were higher than those of Cu–Cu [30]. Rivera et al. found that the average grain size in the deposited AA2219 was 2.5 μm , which is much smaller than that of the base material (30 μm) [31]. Priedeman et al. discovered that the hardness in AFSD of Cu was 62% that of the base material, and they attributed this phenomenon to high density dislocations caused by recrystallization [32]. Phillips et al. pointed out that the β'' precipitates were dissolved and then reprecipitated as Mg–Si solute clusters in the deposited material [33]. Perry et al. found that both AA2024 and AA6061 underwent continuous DRX during AFSD; recrystallization is almost complete in AA2024. Nevertheless, partial recrystallization occurred in AA6061, causing a portion of the low-angle boundaries (LABs) become high-angle boundaries (HABs) [34].

In this work, the first single-layer deposition of AA5B70 was fabricated using AFSD method. The microstructure evolution of the first deposited layer is of utmost importance, which determines the reliability of the subsequent deposited layers, since the subsequent deposition process imposes complex thermo-mechanical coupling effects on the first layer of the build. Therefore, the focus was given to the microstructure and mechanical properties of the first layer of this alloy deposited by the AFSD in the present investigation.

2 Experimental details

AA5B70 was used for both the feedstock and the substrate in the present investigation, whose chemical components and mechanical properties are listed in Tables 1 and 2, respectively. A schematic of the AFSD process is shown in Fig. 1. The feedstock rod was deposited onto the substrate through a hollow and rotating tool (inner diameter 14 mm, outer diameter 28 mm) in this investigation. The AFSD process was performed using a rotating speed of 1500 r/min and a translating speed of 50 mm/min along the rolling direction of the substrate. This experiment was conducted under the displacement control mode, and the distance between the tool head and the substrate was constant (1 mm) during

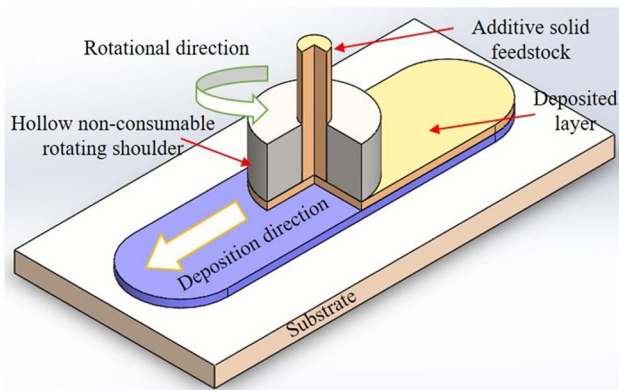


Fig. 1 Schematic illustrations of additive friction stir deposition (AFSD) process

Table 1 Chemical composition of the investigated alloy (wt%)

Element	Mg	Mn	Sc	Zr	Ti	Fe	Si	Al
Content	6.15	0.31	0.30	0.15	0.027	0.09	0.068	Bal

Table 2 Mechanical properties of 5B70 alloy

Tensile strength (MPa)	Yield strength (MPa)	Elongation (%)
440	350	19

the whole AFSD process. Specimens used for performing microstructural examination and hardness tests were cross-sectioned perpendicular to the travel direction using water jet cutting. After that, the specimens were grinded, polished, and then etched with Keller's reagent (2 ml HCl + 3 ml HF + 5 ml HNO₃ + 195 ml H₂O) for 240 s and subsequently observed under optical microscope (OM, OLYMPUS GX71), Electron back scattered diffraction (EBSD, ZEISS Gemini 500) for grain size, and recrystallize analysis in the zones of the deposition. Specimen preparation for EBSD analysis consisted of grinding, mechanical polishing, and then electropolishing with a mixture solution of 10% HNO₃ and 90% C₂H₅OH for 20 s at 15 V and 0 °C. Acquisition of the EBSD data was conducted by ZEISS Gemini 500 field emission scanning electron microscope (SEM) equipped with EBSD attachment.

Vickers microhardness measurements were conducted at the cross-section of the deposition layer under a load of 100 g and a dwell time of 15 s (the equipment model is WHVS-1 M-XYZF). Hardness distribution mapping was obtained by measuring the hardness in the whole cross-section of the deposition layer with an interval of 0.5 mm. The location and configuration of the tensile testing specimens are schematically shown in Fig. 2a, whose geometry and dimensions were designed according to non-standard tensile specimens (see Fig. 2b). Tensile testing was carried out using an in situ dynamic mechanical test system at room temperature, with a cross head speed of 0.5 mm/min. Digital image correlation (DIC, IBTC-5000) technique was used to investigate the local strain distribution and plastic deformation of specimens. Three samples were used for the DIC testing both in the longitudinal and transverse directions. Specimens are sandpapered smooth and then sprayed with white and black lacquer on their surfaces to ensure accurate image resolution. After DIC testing, fractured surfaces are observed by SEM to analyze the fracture pattern of the deposited area and the BM.

3 Results and discussion

3.1 Microstructure evolution

The whole cross-sectional macrostructure and local high magnification microstructure of the deposition fabricated by AFSD are shown in Fig. 3. It can be observed from Fig. 3a that the boundary between the deposition and the substrate can be clearly identified, which presents a wavy-shaped appearance, and a sink was observed in the center of the deposition. The edge of the deposition is not combined with the substrate because the material is extruded by the tool head, and there is no radial and lateral constraint. The heat generation in this area is insufficient, but the heat dissipation is fast, which leads to the poor combination at the edge and the substrate. Porosities can be observed in the enlarged view of point A in Fig. 3a, which can be attributed to insufficient heat generation at this location. Obvious traces of deposited material flow can be observed in Fig. 3b, e, and f, where the material has a large linear velocity. As shown in Fig. 3f, the material flow patterns are rather complex. An unbound boundary line can be clearly identified in Fig. 3c, since the material at the edge has flipped upward under the strong mechanical action of the tool head. Figure 3d shows a high magnification of the central region of the deposition, where uniform and fine grains can be observed [35].

EBSD was applied to investigate the details of grain and texture variation in the AFSD deposition and BM. Figure 4a, c, e, and g shows the inverse pole figures (IPFs) of BM and specific regions of AFSD deposition. The white lines represent low-angle grain boundaries (LAGBs) with a misorientation angle of 2–15°, and the black lines represent high-angle grain boundaries (HAGBs) with a misorientation angle greater than 15°. Figure 4b, d, f, and h shows the pole figures of BM and specific regions of AFSD deposition. The X_0 direction represents the shear

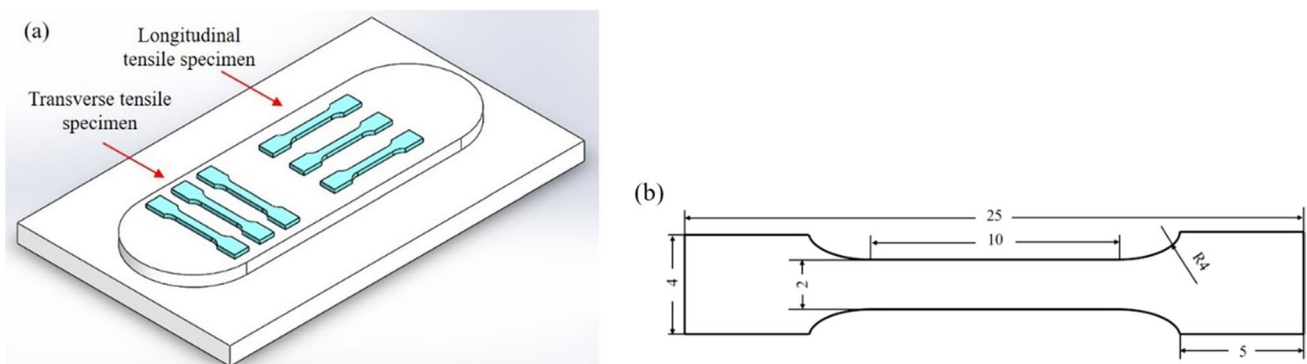
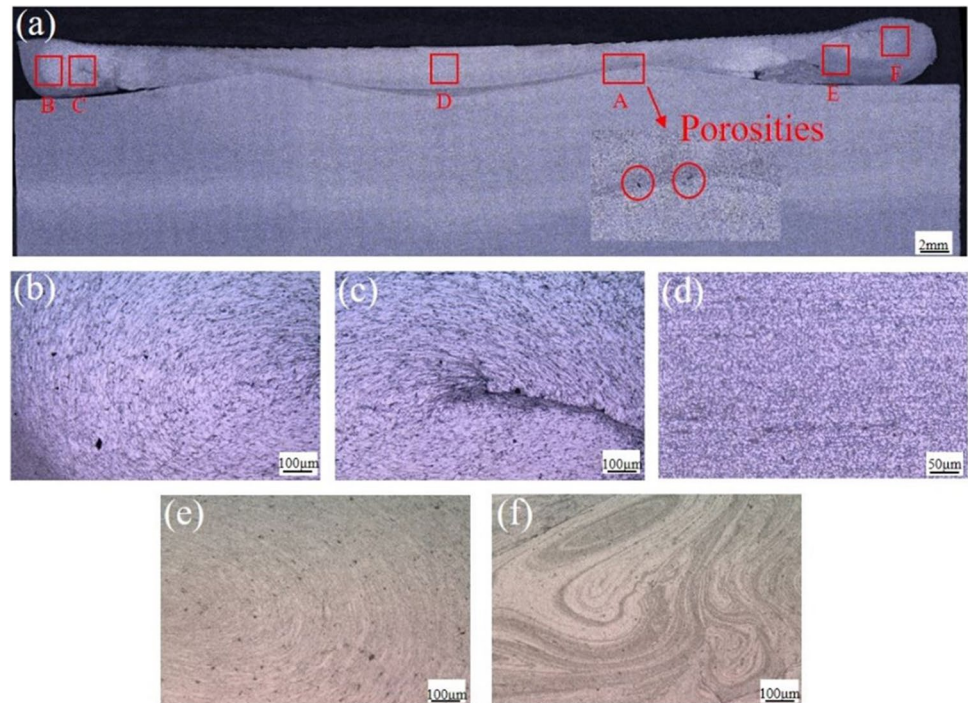


Fig. 2 a Schematic illustration of the location and configuration of the specimens; b geometry and dimensions of tensile specimen

Fig. 3 Optical micrographs of deposition: **a** cross-section of deposition and substrate; **b** zone B; **c** zone C; **d** zone D; **e** zone E; **f** zone F



direction, and the Y_0 direction represents the shear plane normal. The evolution of the texture is described using the density of pole figures given as multiples of uniform distribution (mud). Figure 5 shows the average misorientation angles of BM and specific regions of AFSD deposition.

Figure 4a shows that the grains in BM present an elongated shaped appearance, which are much larger than those in the deposited area, and exhibit a more uniform grain orientation, which is related to the roll forming process. As shown in Fig. 4c, e, and g, the microstructural changes in the upper and lower middle parts of the cross-section of deposition and the edge of the deposition are obvious, and fine equiaxed grains are observed in these regions, indicating that DRX occurred during the deposition process. It can be observed from the EBSD maps that the grain size at the top is larger than those at the bottom, since the heat in the deposited material directly contacts the substrate dissipates more faster than that on the top where the deposited material is exposed to the air. The results show that temperature gradient has great impact on grain size. Figure 4g presents the grain characteristics at the edge of the deposited material, where partial fragmentation of the grains occurred under the strong thermomechanical coupling effect imposed by the rotating tool. The grain orientation is more uniform in this region, where the material is influenced by the rotation of the tool head, which is consistent with the grain characteristic in Fig. 3d.

As shown in Fig. 4b, the texture in BM exhibits strong consistency, but the maximum texture densities in Fig. 4c, e, and g are 2.57, 1.77, and 4.88, respectively (see Fig. 4d, f,

and h), indicating that the texture is rather weak and random in the middle of the deposition due to the random distribution of DRX grains. However, the texture density at the edge of the deposition is much higher, indicating the material in this region has a more consistent flow direction under the stirring action of the tool head.

Figure 5 shows the average misorientation angles of the corresponding region in the EBSD diagram, and the ratios of HAGB in the four areas are 11.36%, 58.74%, 69.82%, and 44.09%, respectively. This set of data is consistent with the previous results of the IPFs of EBSD; the ratio of HAGB reaches a maximum at the bottom, indicating the highest degree of DRX occurred in this region. The degree of DRX at the top is second only to the bottom, but the proportion is also more than 50%, while the ratio of HAGB at the edge of the deposition is less than 50%. In addition, the BM has the highest proportion of subcrystals, and a large number of dislocations were generated during the AFSD processing, while the material undergoes complex thermo-mechanical coupling, and thus, the proportion of HAGB is significantly higher.

3.2 Mechanical performance

As a non-heat treatable aluminum alloy, hardness of 5B70 aluminum alloy is mainly determined by work hardening, i.e., whose hardness is affected by plastic deformation and thermal cycling in the AFSD process. Figure 6 shows the hardness distribution of the cross-section of the AFSD build. In general, the hardness of the cross-section of a build

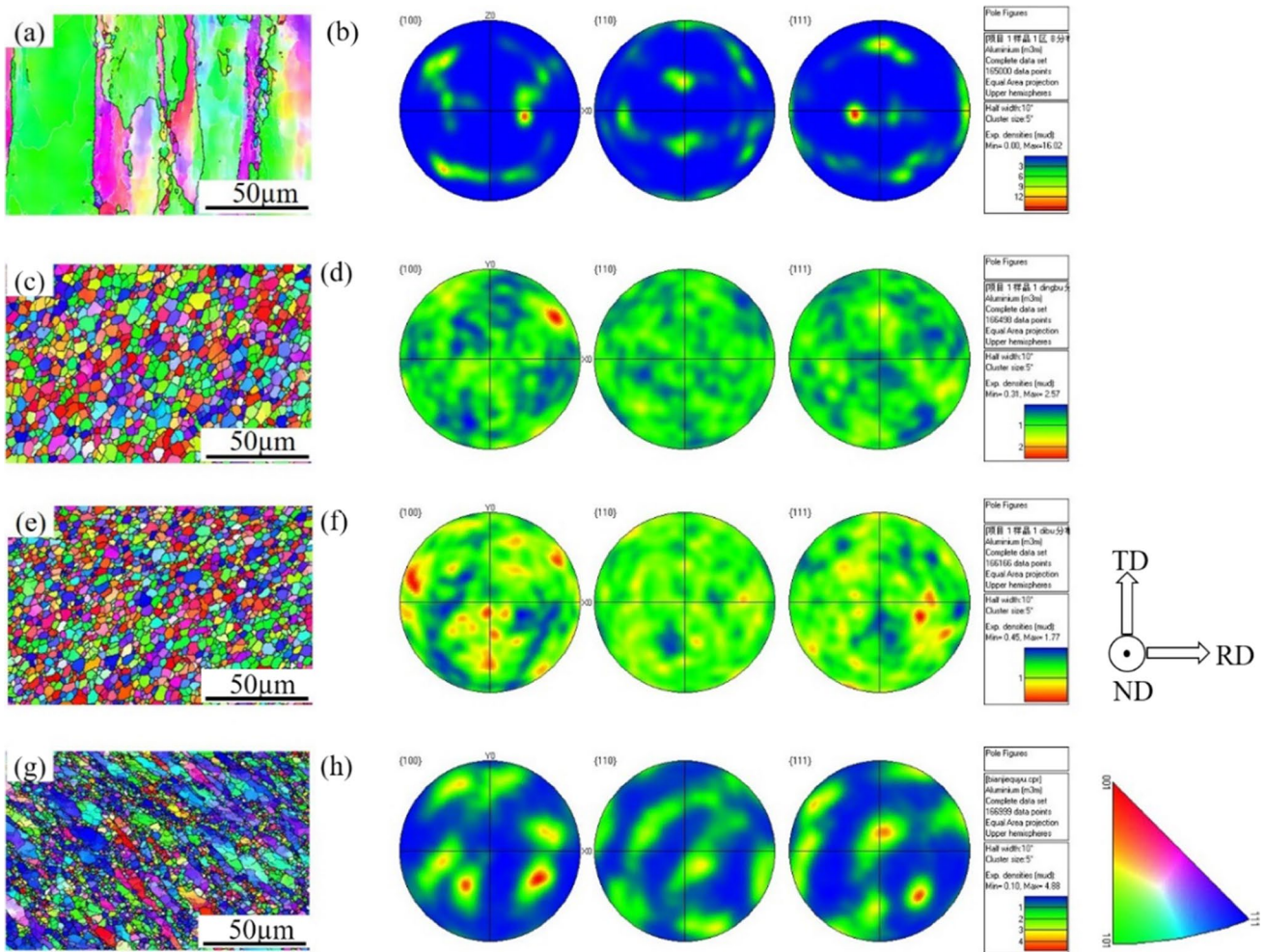


Fig. 4 IPFs and PFs of specimens: **a** IPF of BM; **b** PF of BM; **c** IPF of upper middle part of the cross-section of deposition; **d** PF of upper middle part of the cross-section of deposition; **e** IPF of lower middle

part of the cross-section of deposition; **f** PF of lower middle part of the cross-section of deposition; **g** IPF of the edge of the cross-section of deposition; **h** PF of the edge of the cross-section of deposition

decreases with increasing heat input since the DRX causes a significant decrease in dislocation density, which in turn weakens the effect of work hardening. It is interesting to be noted that no significant gradient of hardness distribution can be observed in the thickness direction, since the build is only approximately 1 mm thick and subjected to only one thermal cycle.

In this work, the DIC technique was applied to investigate the overall strain history of the specimen under tensile loadings. Real-time photographs were taken of the specimens undergoing load testing throughout the test period. Figure 7 shows the strain distribution states of each sample during the whole the testing operation. Figure 7a shows the strain profiles of the BM obtained under different loading levels, indicating that the plastic deformation is uniform at the beginning of loading, and this phenomenon is determined by the uniform microstructure of the BM. As the load increases, the strain is gradually concentrated on one side

until it fractures. Figure 7b, c shows the strain distribution of the specimens in the transverse and longitudinal directions during loading, respectively. It can be observed that the plastic deformation appears to be non-uniform in both directions. Combined with Fig. 7, it can be concluded that the non-uniformity of the plasticity of the specimens in the transverse and longitudinal directions can be attributed to the non-uniformity of their mechanical properties.

It can be observed from Fig. 8 that the strength of the AFSD build is lower than that of the BM in both transverse and longitudinal directions, while the toughness of the AFSD build exceeds that of the BM. Table 3 shows the mechanical properties of specimens. The ultimate tensile strength (UTS) of the AFSD build is 350 MPa in the transverse direction, which is 20% lower than that of the BM, and the elongation is 22%, which is 16% higher than that of the BM. The UST longitudinal specimen is 276 MPa, which is 37% lower than that of the BM, and the elongation is 27%,

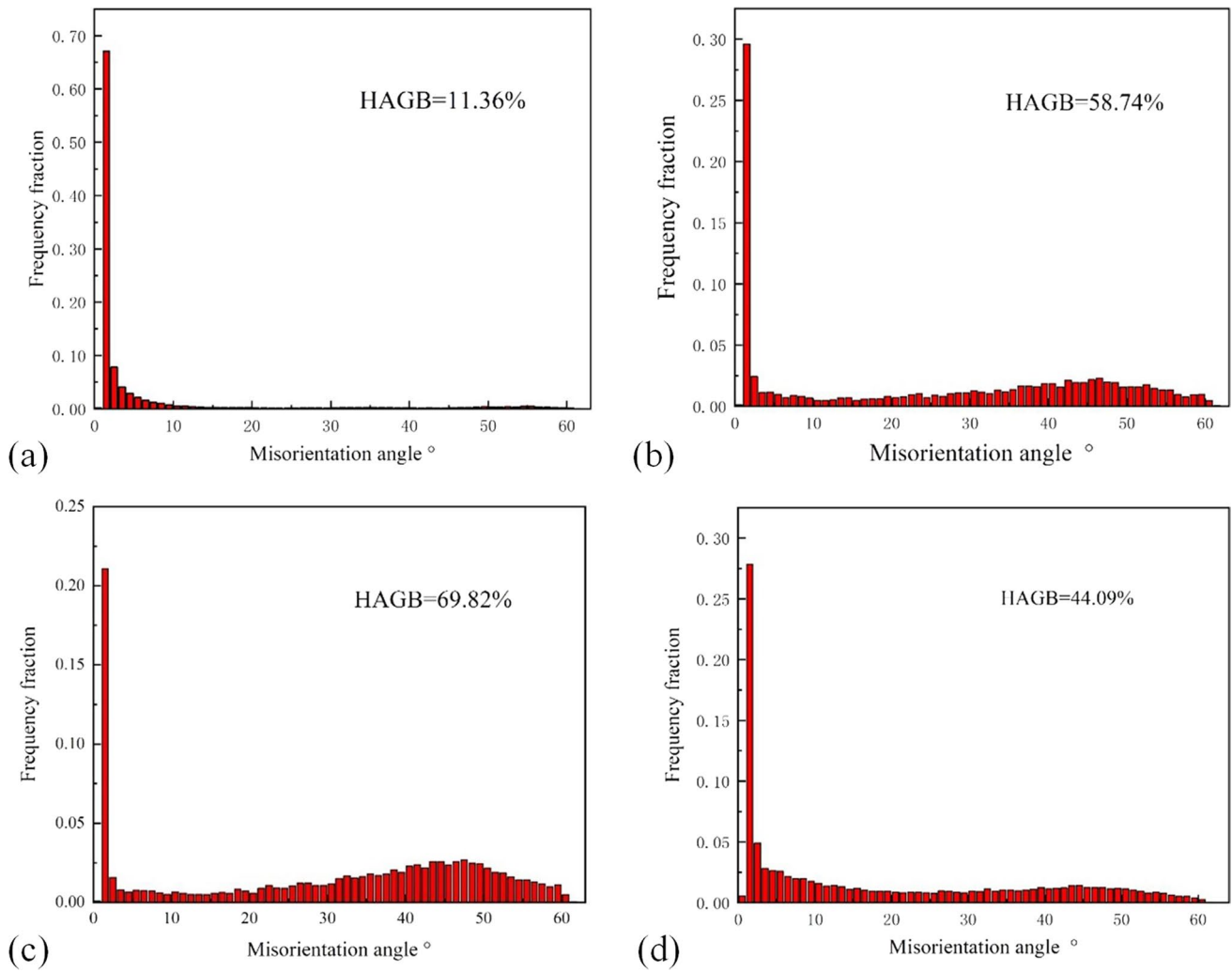
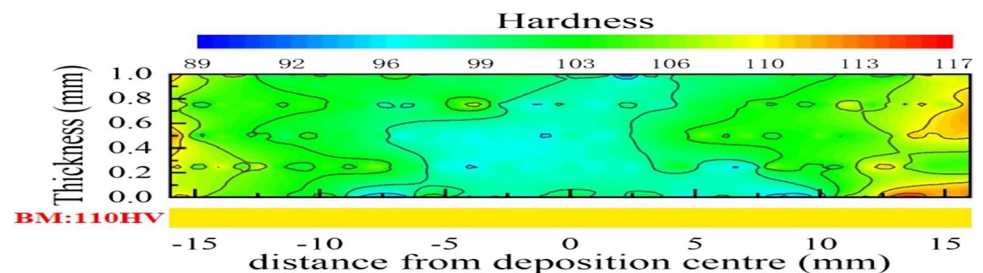


Fig. 5 The misorientation angle of specimens: **a** BM; **b** upper middle part of the cross-section of deposition; **c** lower middle part of the cross-section of deposition; **d** the edge of the cross-section of deposition

Fig. 6 Microhardness nephogram of the component



which is 42% higher than that of the BM. Combined with Figs. 4 and 5, the deposited material has finer grains and a higher percentage of HAGB, which impede crack extension and improve the material's ability to absorb energy from the fracture process, thus improving their toughness compared to that of the BM in both transverse and longitudinal directions.

As shown in Fig. 9, after the tensile testing, the microscopic morphology of the fracture of each specimen was observed using SEM. The microscopic morphology of the fractures of all specimens shows numerous dimples, while the dimples are more dense and deeper in Fig. 9b, c, indicating that the transverse and longitudinal specimens experienced more severe plastic deformation before the failure,

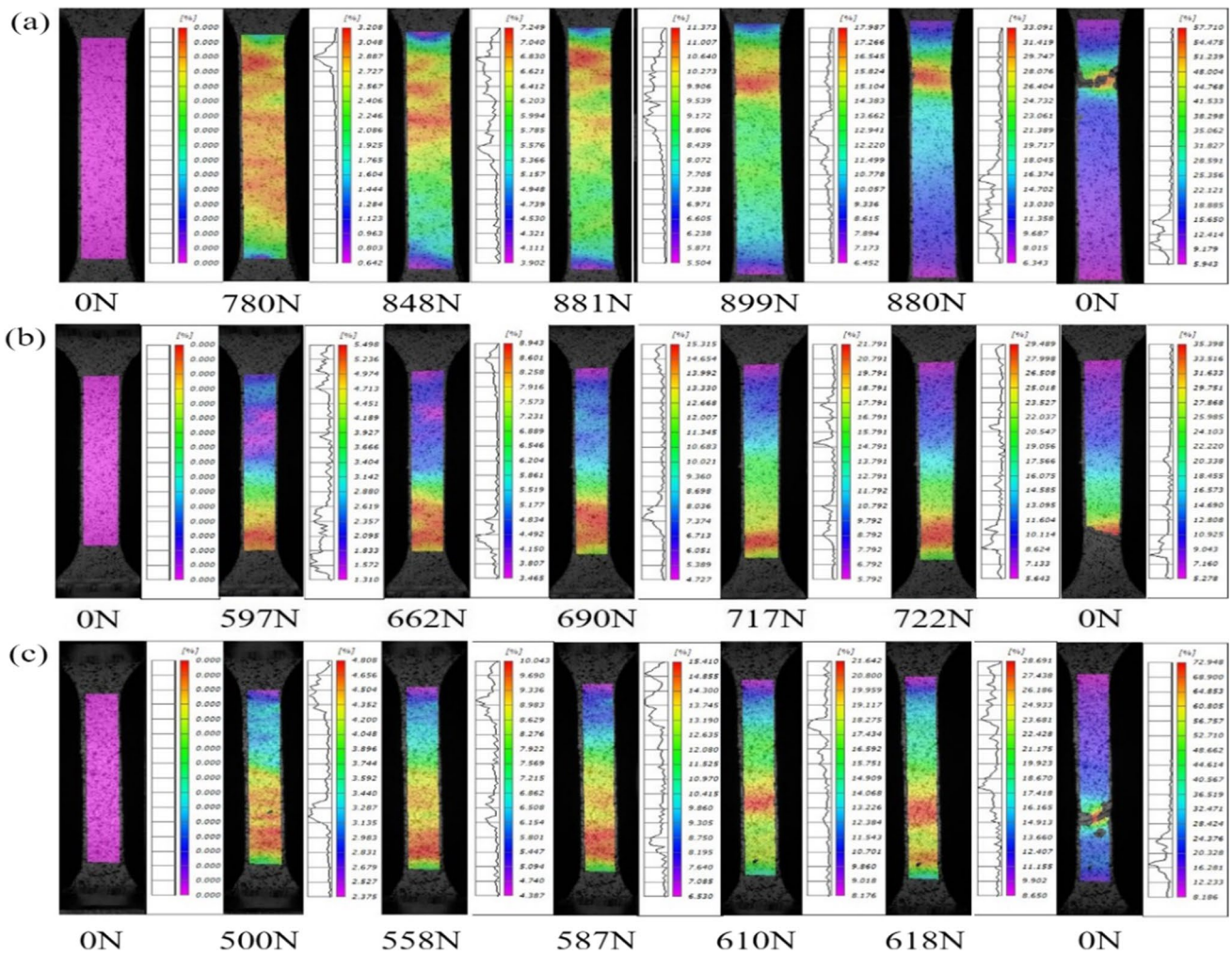


Fig. 7 The strain state of specimens in successive loading: **a** BM; **b** transverse specimen; **c** longitudinal specimen

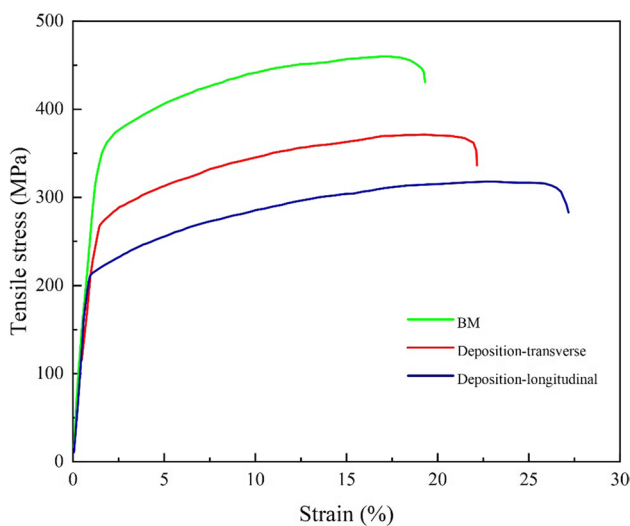


Fig. 8 The stress–strain curve of the specimens

Table 3 Mechanical properties of specimens

	Tensile strength (MPa)	Yield strength (MPa)	Elongation (%)
Transverse	350	260	22
Longitudinal	276	210	27

whose toughness is better since the fine equiaxed grains were formed via recrystallization.

4 Conclusions

AFSD is a relatively new solid-state additive technology. In this work, a layer of aluminum alloy material was successfully deposited on the substrate, whose microstructure and

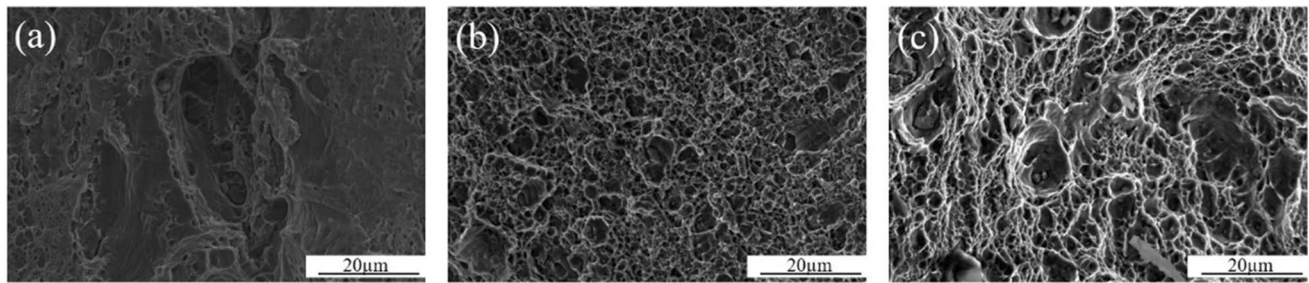


Fig. 9 Fracture surface of specimens: **a** BM; **b** transverse specimen; **c** longitudinal specimen

mechanical properties were systematically investigated, and the conclusions are as follows:

- (1) The interface between the deposited layer and the substrate presents a wave-shaped appearance, porosities are observed in some local areas, and a large number of flashes are generated in this area due to the lack of lateral axial restraint at the edges of the deposition layer.
- (2) The grains in the BM show an elongated-shaped appearance with a more uniform orientation and a large number of subcrystalline structures due to the rolling process. In the cross-section of the deposition layer, the degree of recrystallization in the central region is relatively high, where the grains are fine, the percentage of HAGB is more than 50%, and the texture orientation is random. Nevertheless, the material in the edge position flows with the rotation of the tool head, and the grains are not uniformly distributed.
- (3) The hardness in the cross-section of the deposition layer presents a gradient distribution, with a 10% reduction of hardness in the central region compared to that at the edge regions. When tensile tests were performed on both transverse and longitudinal specimens of the deposition layer, the strain distribution was found to be non-uniform, indicating the existence of a mechanical property gradient in both directions. In addition, the strength in the transverse and longitudinal specimens decreased by 20% and 37%, respectively, while the elongation increased by 16% and 42%. It was found that all specimens showed ductile fracture with the presence of tough nests, while the distribution of dimples in the deposition was more dense and deeper where the material experienced more intense plastic deformation.

Author contribution All authors contributed to the study conception and design. Material preparation, data collection, and analysis were performed by Zhikang Shen and Mingtao Zhang. The first draft was written by Mingtao Zhang, and Zhikang Shen made correction.

Dongxiao Li did the additive friction stir deposition experiments with the help of Xinyu Liu and Shaolong Chen. Wentao Hou and Zhonggang Sun gave advice for manuscript writing, and Yuquan Ding, Yanhong Tian, and Wenya Li guided the analysis. All authors read and approved the final manuscript.

Funding This work was funded by the National Natural Science Foundation of China (nos. 52174374 and 51975479), Chinese National Natural Science Foundation-“Chi-Sun Yeh” Science Foundation (no. U2241248), Xi’an City Science and Technology Bureau Project (no. 21XJZZ0080), and State Key Laboratory of Advanced Welding and Joining, Harbin Institute of Technology (no. AWJ-23M15).

Declarations

Competing interests The authors declare no competing interests.

References

1. Blakey-Milner B, Gradl P, Snedden G, Brooks M, Pitot J, Lopez E, Leary M, Berto F, Plessis AD (2021) Metal additive manufacturing in aerospace: a review. *Mater Des* 209:110008
2. Motallebi R, Savaedi Z, Mirzadeh H (2022) Additive manufacturing – a review of hot deformation behavior and constitutive modeling of flow stress. *Curr Opin Solid State Mater Sci* 26(3):100992
3. Rathee S, Srivastava M, Pandey PM, Mahawar A, Shukla S (2021) Metal additive manufacturing using friction stir engineering: a review on microstructural evolution, tooling and design strategies. *CIRP J Manuf Sci Technol* 35:560–588
4. Shen Z, Chen S, Cui L, Li D, Liu X, Hou W, Chen H, Sun Z, Li W (2022) Local microstructure evolution and mechanical performance of friction stir additive manufactured 2195 Al-Li alloy. *Mater Charact* 186:111818
5. Chen H, Sun Y, Yuan W, Pang S, Yan W, Shi Y (2022) A review on discrete element method simulation in laser powder bed fusion additive manufacturing. *Chin J Mech Eng: Additive Manufacturing Frontiers* 1(1):100017
6. Mostafaei A, Zhao C, He Y, Ghiaasiaan SR, Shi B, Shao S, Shamsaei N, Wu Z, Kouraytem N, Sun T, Pauza J, Gordon JV, Webler B, Parab ND, Asherloo M, Guo Q, Chen L, Rollett AD (2022) Defects and anomalies in powder bed fusion metal additive manufacturing. *Curr Opin Solid State Mater Sci* 26(2):100974
7. Astafurov S, Astafurova E, Reunova K, Melnikov E, Panchenko M, Moskvina V, Maier G, Rubtsov V, Kolubaev E (2021) Electron-beam additive manufacturing of high-nitrogen steel: microstructure and tensile properties. *Mater Sci Eng, A* 826:141951
8. Chen J, Fabijanic D, Zhang T, Lui E, Brandt M, Xu W (2022) Deciphering the transformation pathway in laser powder-bed

- fusion additive manufacturing of Ti-6Al-4V alloy. *Addit Manuf* 58:103041
9. Lin Z, Song K, Yu X (2021) A review on wire and arc additive manufacturing of titanium alloy. *J Manuf Process* 70:24–45
 10. Srivastava M, Rathee S, Maheshwari S, Noor Siddiquee A, Kundra TK (2019) A review on recent progress in solid state friction based metal additive manufacturing: friction stir additive techniques. *Crit Rev Solid State Mater Sci* 44(5):345–377
 11. James S, Dang C (2020) Investigation of shear failure load in ultrasonic additive manufacturing of 3D CFRP/Ti structures. *J Manuf Process* 56:1317–1321
 12. Ren Y, Liu H, Zhao L, Cui X, Shen Y, Wang J, Xiong T (2021) Study of microstructural and mechanical anisotropy of 7075 Al deposits fabricated by cold spray additive manufacturing. *Mater Des* 212:110271
 13. Srivastava AK, Kumar N, Dixit AR (2021) Friction stir additive manufacturing—an innovative tool to enhance mechanical and microstructural properties. *Mater Sci Eng, B* 263:114832
 14. Mason C, Rodriguez RI, Avery DZ, Phillips BJ, Bernarding BP, Williams M, Cobbs SD, Jordon JB, Allison PJ (2021) Process-structure-property relations for as-deposited solid-state additively manufactured high-strength aluminum alloy. *Addit Manuf* 40:101879
 15. Gopan V, Wins KLD, Surendran A (2021) Innovative potential of additive friction stir deposition among current laser based metal additive manufacturing processes: a review. *CIRP J Manuf Sci Technol* 32:228–248
 16. Yu HZ, Mishra RS (2021) Additive friction stir deposition: a deformation processing route to metal additive manufacturing. *Mater Res Lett* 9(2):71–83
 17. Elfishawy E, Ahmed M, El-Sayed Seleman M (2020) Additive manufacturing of aluminum using friction stir deposition. *TMS 2020 149th Annual Meeting & Exhibition Supplemental Proceedings* 227–238
 18. Rivera O, Allison P, Jordon J, Rodriguez O, Brewer L, McClelland Z, Whittington W, Francis D, Su J, Martens RL, Hardwick N (2017) Microstructures and mechanical behavior of Inconel 625 fabricated by solid-state additive manufacturing. *Mater Sci Eng, A* 694:1–9
 19. Nasiri AM, Shen Z, Hou JSC, Gerlich AP (2018) Failure analysis of tool used in refill friction stir spot welding of Al 2099 alloy. *Eng Fail Anal* 84:25–33
 20. Ni Y, Fu L, Shen Z, Liu XJ (2019) Role of tool design on thermal cycling and mechanical properties of a high-speed micro friction stir welded 7075–T6 aluminum alloy. *J Manuf Process* 48:145–153
 21. Shen Z, Li W, Ding Y, Hou W, Liu X, Guo W, Chen H, Liu X, Yang J, Gerlich AJ (2020) Material flow during refill friction stir spot welded dissimilar Al alloys using a grooved tool. *J Manuf Process* 49:260–270
 22. Zhao H, Shen Z, Booth M, Wen J, Fu L, Gerlich A (2018) Calculation of welding tool pin width for friction stir welding of thin overlapping sheets. *Int J Adv Manuf Technol* 98(5):1721–1731
 23. Shen Z, Ding Y, Guo W, Hou W, Liu X, Chen H, Liu F, Li WY, Gerlich A (2021) Refill friction stir spot welding Al alloy to copper via pure metallurgical joining mechanism. *Chin J Mech Eng* 34(1):1–8
 24. Stubblefield G, Fraser K, Phillips B, Jordon J, Allison PJ (2021) A meshfree computational framework for the numerical simulation of the solid-state additive manufacturing process, additive friction stir-deposition (AFS-D). *Mater Des* 202:109514
 25. Shen Z, Ding Y, Gerlich AP (2020) Advances in friction stir spot welding. *Crit Rev Solid State Mater Sci* 45(6):457–534
 26. Anderson-Wedge K, Avery D, Daniewicz S, Sowards J, Allison P, Jordon J, Amaro R (2021) Characterization of the fatigue behavior of additive friction stir-deposition AA2219. *Int J Fatigue* 142:105951
 27. Joshi SS, Patil SM, Mazumder S, Sharma S, Riley DA, Dowden S, Banerjee R, Dahotre NB (2022) Additive friction stir deposition of AZ31B magnesium alloy. *J Magnes Alloys* 10(9):2404–2420
 28. Garcia D, Hartley WD, Rauch HA, Griffiths RJ, Wang R, Kong ZJ, Zhu Y, Hang ZY (2020) In situ investigation into temperature evolution and heat generation during additive friction stir deposition: a comparative study of Cu and Al-Mg-Si. *Addit Manuf* 34:101386
 29. Mironov S, Inagaki K, Sato Y, Kokawa H (2015) Microstructural evolution of pure copper during friction-stir welding. *Phil Mag* 95(4):367–381
 30. Griffiths RJ, Garcia D, Song J, Vasudevan VK, Steiner MA, Cai W, Hang ZY (2021) Solid-state additive manufacturing of aluminum and copper using additive friction stir deposition: process-microstructure linkages. *Materialia* 15:100967
 31. Rivera O, Allison P, Brewer L, Rodriguez O, Jordon J, Liu T, Whittington W, Martens R, McClelland Z (2018) Influence of texture and grain refinement on the mechanical behavior of AA2219 fabricated by high shear solid state material deposition. *Mater Sci Eng, A* 724:547–558
 32. Priedeman JL, Phillips BJ, Lopez JJ, Tucker Roper BE, Hornbuckle BC, Darling KA, Jordon JB, Allison PG, Thompson GB (2020) Microstructure development in additive friction stir-deposited Cu. *Metals* 10(11):10111538
 33. Phillips B, Avery D, Liu T, Rodriguez O, Mason C, Jordon J, Brewer L, Allison P (2019) Microstructure-deformation relationship of additive friction stir-deposition Al–Mg–Si. *Materialia* 7:100387
 34. Perry ME, Griffiths RJ, Garcia D, Sietins JM, Zhu Y, Hang ZY (2020) Morphological and microstructural investigation of the non-planar interface formed in solid-state metal additive manufacturing by additive friction stir deposition. *Addit Manuf* 35:101293
 35. McNelley T, Swaminathan S, Su J (2008) Recrystallization mechanisms during friction stir welding/processing of aluminum alloys. *Scripta Mater* 58(5):349–354

Publisher's note Springer Nature remains neutral with regard to jurisdictional claims in published maps and institutional affiliations.

Springer Nature or its licensor (e.g. a society or other partner) holds exclusive rights to this article under a publishing agreement with the author(s) or other rightsholder(s); author self-archiving of the accepted manuscript version of this article is solely governed by the terms of such publishing agreement and applicable law.